Superresolution Land Cover Mapping Using Spatial Regularization

Feng Ling, Xiaodong Li, Fei Xiao, and Yun Du

***Abstract*—Superresolution mapping (SRM) is a method of predicting the spatial locations of land cover classes within mixed pixels in remotely sensed images. This paper proposes a novel SRM framework that is operated from the perspective of spatial regularization. Within the proposed framework, SRM aims to generate final superresolution land cover maps that conform to inputted fraction images, with spatial regularization intended for exploiting *a priori* knowledge about the land cover maps. Two SRM models are constructed by using maximal spatial dependence as the spatial regularization term and the L1 or L2 norm as the data fidelity term. The proposed models are evaluated by using synthetic Landsat, real IKONOS, and real Airborne Visible/Infrared Imaging Spectrometer images and compared with hard classification technologies, as well as pixel-swapping, Hopfield neural network, and Markov random field SRM models. We perform linear spectral mixture analysis (LSMA) and multiple endmember spectral mixture analysis (MESMA) to estimate fraction images. Results show that the accuracy of inputted fraction images plays an important role in the final superresolution land cover maps and that using MESMA fraction images results in higher accuracy than using LSMA fraction images. Moreover, the L-curve criterion is suitable for choosing the optimal regularization parameter in both SRM models. Compared with hard classification technologies and other SRM models, the proposed model derives the highest Kappa coefficients and lowest class area proportion errors when MESMA fraction images are used as input.**

***Index Terms*—Spatial regularization, spectral unmixing, superresolution mapping (SRM).**

I. Introduction

PIXEL mixtures are critical problems encountered when extracting land cover information from remotely sensed images [1]–[3]. A mixed pixel generally cannot be appropriately represented by standard hard classification technologies, which regard one pixel a unit that belongs solely to a single land cover class. By contrast, spectral unmixing or soft classification technologies [4]–[6] do not assign a mixed pixel to a single land cover class but instead generate fraction images that represent proportional areas of different land cover classes within mixed pixels. Spectral unmixing technologies provide more useful land cover information than hard classification technologies. Nevertheless, the actual spatial distribution of each land cover class in mixed pixels cannot be distinguished using spectral unmixing technologies.

Superresolution mapping (SRM), also referred to as subpixel mapping, is a promising method of predicting the spatial distribution of different land cover classes within mixed pixels [7]–[9]. SRM can be considered the postprocessing stage of spectral unmixing, in which the fraction images produced by spectral unmixing are used as input to retrieve a superresolution land cover map with fine spatial resolution. SRM generates a more informative superresolution land cover map than hard classification and spectral unmixing technologies and is a partial solution to the limitations presented by the coarse spatial resolution of remotely sensed images. SRM has been used in many fields, including mapping rural land cover [10]–[12], urban land cover [13], [14], waterlines [15]–[17], and land cover changes [18], as well as refining ground control points [19] and calculating landscape pattern indices [20].

The scientific community currently focuses on primary concerns over the SRM models used to describe the spatial patterns of land cover classes [9]. Once a specific model of spatial patterns is determined, SRM is generally converted into an optimization problem, in which the objective is now to identify a superresolution land cover map that corresponds to the spatial pattern model. Various spatial pattern models have been proposed and used for SRM. The maximal spatial dependence model is extensively used in the H-resolution case, in which image pixels are smaller than the objects of interest [8], [21]–[24]. The variogram [25], [26] and multiple-point geostatistics [27], [28] are used in the L-resolution case, wherein image pixels are larger than the objects of interest. Moreover, additional site-specific data, such as panchromatic images [29], [30], light detection and ranging data [31], digital elevation models [17], high-resolution segmentation images [32] and multitemporal images [33], [34], have been used to provide more information about the spatial patterns of land cover classes and improve the effectiveness of SRM models.

Aside from spatial pattern models, the approach to handling inputted fraction images is another critical factor for SRM. Even though models of land cover spatial patterns and area fraction constraints or the spectral separability of land cover classes both constrain SRM results [35], [36], the latter attract relatively little attention.

The methods for resolving the area fraction constraints in existing SRM models are generally classified into two categories. In the first category, the number of subpixels for each land cover class in each mixed pixel is restricted so that it corresponds with inputted area fractions. Various specific methods

Manuscript received June 12, 2012; revised January 10, 2013 and June 17, 2013; accepted August 31, 2013. This work was supported in part by the National Basic Research Program (973 Program) of China under Grant 2013cb733205 and in part by the Natural Science Foundation of China under Grant 41301398.

The authors are with the Key laboratory of Monitoring and Estimate for Environment and Disaster of Hubei province, Institute of Geodesy and Geophysics, Chinese Academy of Sciences, Wuhan 430077, China (e-mail: lingf@whigg.ac.cn).

Color versions of one or more of the figures in this paper are available online at http://ieeexplore.ieee.org.

Digital Object Identifier 10.1109/TGRS.2013.2281992

have been proposed in different SRM models: 1) in the pixel-swapping model [21]–[24], the number of subpixels is determined according to area fractions inputted in the initialization step, and during the iteration, the subpixel location changes, whereas the number of subpixels remains constant; 2) in the interpolation-based model [37], subpixels are assigned according to interpolated values only if the available subpixels for a particular class have not been completely exhausted, and this pixel assignment approach has also been applied in the SRM models proposed in [38]–[41]; and 3) in the stochastic simulation model, the running probability of each subpixel is considered a function of the number of previously simulated labels of the same class at subpixels within each mixed pixel [25], [27], [28]. In general, maintaining the subpixel numbers is valuable for model development because no extra fraction errors need to be considered [9]. However, given that spectral unmixing is still an open problem and that accurate fraction images are always unavailable in practice [4]–[6], the fraction errors resulting from spectral unmixing considerably affect the performance of SRM with a fixed number of subpixels. Consequently, numerous speckle artifacts may characterize a final superresolution land cover map, thereby giving rise to the need for additional postprocessing steps, such as spatial filtering, to eliminate fraction errors [10].

In the second category, the fractions in a final superresolution land cover map can differ from inputted fraction images. This alternative approach relaxes the constraints caused by fraction images and eliminates the fraction errors caused by spectral unmixing. The widely used Hopfield neural network (HNN)-based SRM model belongs to this category [7], [26], [29], [30], [33]. The HNN model considers SRM an optimization problem, in which the aim is to minimize an energy function with a goal function and two constraints that are balanced by weights. The goal function maximizes the spatial clustering between subpixels and plays the same role as a spatial pattern model. The proportion constraint maintains the proportions in inputted images, and the multiple-class constraint ensures that each class layer can be fitted together with no gaps or overlaps in a final land cover map [12]. The proportion constraint can be relaxed by adjusting the weights between the goal function and constraints, thereby enabling the acquisition of accurate results in the presence of fraction errors. Although the HNN model is widely used, this model still has several limitations. First, fraction images are represented by various interconnected layers in a network. The spatial pattern is calculated only within each layer for individual land cover classes. Thus, the relationships among different land cover classes are disregarded. Second, all the layers in a network must be combined using an additional multiclass constraint to ensure that the result is a categorical field, making the model too complex. Finally, the determination of the weights in the model is usually subjective and without theoretical basis. Aside from the HNN model, Robin *et al.* proposed another SRM model [32], in which both high-resolution structural information and coarse-resolution temporal information were used to generate a superresolution land cover map. The model is based on the linear mixture model for coarse-resolution pixel disaggregation and a high-resolution segmentation image that is used to provide the land cover proportions. Although the model can produce a fine superresolution land cover map, the inputted high-resolution segmentation image is often unavailable in practice, limiting the usage of the model.

In effect, the second category of SRM models can be considered a regularization method. The coarse-resolution fraction images are the only available data to which SRM is applied in reconstructing a final superresolution land cover map. The objective of SRM therefore should be to recover a superresolution land cover map from inputted fraction images. Given that many land cover configurations satisfy area fractions, SRM becomes an ill-posed inversion problem with an insufficient number of observations and a nonunique and unstable solution. To overcome the ill-posed nature of the SRM problem, SRM models convert the ill-posed inversion problem into an optimization problem by defining an object function [7], [8], [23], [42]–[46]. The regularization method is widely regarded as a promising method with which to resolve the aforementioned problem; it has therefore found extensive application in many fields, such as image analysis and pattern recognition [47]–[51]. In its broadest sense, regularization is a mathematical technique that facilitates the use of *a priori* information in the form of a regularization relationship for the solution of ill-posed problems. On the basis of regularization, the objective of SRM is to ensure that retrieved fine-resolution maps conform to coarse-resolution fraction images according to an observation model that connects the maps and images. To convert an ill-posed problem into a well-posed one, regularization exploits *a priori* knowledge about a land cover map. Therefore, SRM performed from the perspective of a regularization problem can be relevant when a unified framework is required to reconstruct a final superresolution land cover map from inputted fraction images by SRM.

Several SRM models are directly applied to images by using spectral constraints instead of the proportion constraints provided by fraction images. These models, which include the Markov random field (MRF) [36], [52], [53], spectral–spatial integration [54], and fuzzy c-means [55], are established upon regularization. Despite the advantage of this approach, however, replacing proportion constraints with spectral constraints poses serious limitations. The spectral constraint used in the aforementioned models is the object function of certain spectral unmixing algorithms, such as the Gaussian maximum likelihood algorithm in the MRF model and the linear unmixing algorithm used in the spectral–spatial integration model. Thus, the spectral unmixing algorithm incorporated into the SRM model has an important impact on the derived results. Nonetheless, only simple spectral unmixing algorithms have thus far been used. Powerful spectral unmixing algorithms, such as the nonlinear spectral unmixing algorithm and multiple endmember spectral unmixing algorithm, are difficult to apply, limiting their use in SRM models. By contrast, the SRM model that uses fraction images as input is independent of the spectral unmixing algorithm. Any spectral unmixing algorithm can be used as a preprocessing tool for estimating fraction images, thereby generating corresponding SRM models that are flexible in practice.

This paper proposes a novel SRM framework that is operated under a regularization perspective. The proposed framework

is easy to implement and eliminates the errors resulting from inputted fraction images. The rest of this paper is organized as follows. Section II presents the problem formulation and proposed approach. Section III discusses the implementation of the proposed approach, along with the experimental results on synthetic and real images. Section IV concludes this paper.

II. Methodology

A. Modeling the SRM Problem

We assume that a remotely sensed image with coarse spatial resolution has $M_1 \times M_2$ pixels and that the number of land cover classes in the entire image is C. Let Y be the fraction images yielded by spectral unmixing; it is denoted in vector form as $Y = [y_1^1, y_2^1 \dots y_{M_1 \times M_2}^1, y_1^2, y_2^2 \dots y_{M_1 \times M_2}^2 \dots y_{M_1 \times M_2}^C]$, where y_V^c is the fraction value of the cth class in coarse-resolution pixel V. By setting the zoom factor as z and using Y as input, SRM aims to generate a labeled land cover map $X = [x_1, x_2 \dots x_{(z \times M_1) \times (z \times M_2)}]$, where $(z \times M_1) \times (z \times M_2)$ is the size of the resultant fine-resolution land cover map. All the subpixels in X are considered pure pixels and should be assigned to a certain land cover class as $x_v \in (1, \dots C)$ for subpixel v. Each coarse-spatial-resolution pixel V corresponds to a specific $z \times z$ patch in X. Therefore, y_V^c is the percentage of the subpixels assigned to land cover class c in this patch. This percentage can be calculated as

$$y_V^c = \sum_{v \in V} \varphi_{(x_v = c)} / z^2 \tag{1}$$

where $\varphi_{(x_v=c)} = 1$ if subpixel x_v is the cth land cover class; otherwise, $\varphi_{(x_v=c)} = 0$. On the basis of all the land cover classes in the entire image, the general observation model for SRM can be represented as follows:

$$Y = HX + N \tag{2}$$

where $[C \times M_1 \times M_2, (z \times M_1) \times (z \times M_2)]$ matrix H is the subsampling matrix that represents the degradation process between X (of size $[(z \times M_1) \times (z \times M_2), 1]$) and Y (of size $[C \times M_1 \times M_2, 1]$), similar to the form of (1). $[C \times M_1 \times M_2, 1]$ matrix N represents the fraction errors caused by spectral unmixing.

As indicated in the observation model defined in (2), a popular method of estimating the corresponding fine-resolution land cover map from observed coarse-resolution fraction images is the maximum likelihood-type estimator. The definition of the estimator in the SRM context can be expressed as the following minimization problem:

$$\widehat{X} = \arg\min_x D(X, Y, H) \tag{3}$$

where $D(X, Y, H)$ is a data fidelity term that represents the inconsistency between X and Y; minimizing $D(X, Y, H)$ provides a conformance force of X to Y, according to the observation model used.

Mathematically, the problem of recovering X from Y is an ill-posed inverse problem because the basic observation model corresponds to an underdetermined linear system with infinite possible solutions. Regularization can be included in the cost function to stabilize the problem or constrain the space of solutions. Traditionally, regularization takes the form of constraints in the space of possible solutions, which is often independent of measured data. On the basis of *a priori* knowledge on the spatial patterns of land cover, therefore, SRM uses regularization techniques to approximate superresolution land cover map X. In this approximation, SRM considers the following united framework:

$$\widehat{X} = \arg\min_x [D(X, Y, H) + \lambda R(X)] \tag{4}$$

where $R(X)$ is a regularization term that explicitly takes *a priori* information on superresolution land cover map X into account, and λ is a global weight parameter that balances the contribution of regularization and data fidelity terms.

To construct a specific SRM model within the regularization framework, the data fidelity term $D(X, Y, H)$, the regularization term $R(X)$, and a suitable regularization parameter λ for balancing both terms should be chosen.

B. Data Fidelity Term

The data fidelity term represents the closeness of a final solution to measured data. For SRM, the final solution is the superresolution land cover map, and the measured data are the fraction images extracted by spectral unmixing. Therefore, a cost function should be defined to measure the difference between the area percentage in the final superresolution land cover map and the inputted fraction images. We investigate L2 and L1 norm estimators, which are commonly used for the data fidelity term [56].

A common cost function is the least squares cost function, which minimizes the L2 norm of the residual vector. Thus

$$D(X, Y, H) = \|Y - HX\|_2^2. \tag{5}$$

In cases wherein N is the additive white zero-mean Gaussian noise, the L2 norm approach provides the maximum likelihood estimate of data.

Another widely used cost function is the L1 norm, which is the maximum likelihood estimate of data in the presence of Laplacian noise

$$D(X, Y, H) = \|Y - HX\|_1. \tag{6}$$

The robustness of an employed estimator is key to SRM results. In general, the choice of the data fidelity term should correspond with the features of noise included in inputted fraction images. In later experiments, we compare the performance of the L2 and L1 norms as the data fidelity terms.

C. Regularization Term

To estimate the final result, particular knowledge regarding the spatial patterns of land cover classes should be obtained through regularization. For SRM, the spatial dependence principle (i.e., the tendency for spatially proximate observations

of a given property to be more similar to one another than distant observations) is the most popular model used to describe the spatial patterns of land cover. In this paper, the spatial dependence principle is used as the prior model of land cover maps. This principle is identical to the smoothness principle, which is widely used for spatial regularization. Both principles aim to create neighboring pixels that have the same labels.

Considering a neighboring window $w \times w$ for each subpixel x_v, the regularization term $R(X)$ is calculated as

$$R(X) = \sum_{v=1}^{(z\times M_1)\times(z\times M_2)} R(x_v) = \sum_{v=1}^{(z\times M_1)\times(z\times M_2)} \sum_{n=1}^{w\times w} \phi_n \times \delta(x_v, x_n) \quad (7)$$

where $\delta(x_v, x_n)$ characterizes the relationship between the subpixel x_v and its neighboring subpixels x_n. Neighboring land cover classes more likely share the same properties than those distantly located from one another; furthermore, the spatial dependence principle should contribute to the minimal value suitable for the framework in (4). Thus, $\delta(x_v, x_n)$ is defined as

$$\delta(x_v, x_n) = \begin{cases} 0 & \text{if } x_v = x_n \\ 1 & \text{otherwise} \end{cases} \quad (8)$$

with ϕ_n as the spatial weighting function that balances the influence of the subpixel x_n

$$\phi_n = (d(x_v, x_n))^{-\kappa} \quad (9)$$

where $d(x_v, x_n)$ is the distance between subpixels x_v and x_n and κ is the power law index that controls the nonlinear parameter of the distance decay model.

D. Determination of Regularization Parameters

Regularization parameter λ acts as a tradeoff parameter that balances the influence of the data fidelity and regularization terms on the solution of (4). If the regularization parameter is too low, the solution is unsmoothed and susceptible to the noise in inputted fraction images. Otherwise, the regularization term has a dominant effect on the solution, generating an oversmoothed superresolution land cover map. The data fidelity and regularization terms should be appropriately balanced when the SRM model based on regularization is implemented. A number of selecting rules, such as L-curve method [48], [49] and generalized cross-validation [57], [58], have been proposed for identifying the optimal value of the regularization parameter.

In this paper, the L-curve method is used to determine the optimal value of λ [48], [49]. This method does not require any *a priori* knowledge of noise level, making it a fully data driven approach. It has been popular since its inception and has shown satisfactory performance in many practical inverse problems. This method is a graphical tool for analysis. It shows the relationship between the data fidelity and regularization terms, which are $D(X, Y, H)$ and $R(X)$, respectively [see (4)]. For a given λ, the values of both terms are calculated from the final superresolution land cover map. When these values are plotted on a log-log scale for a range of λ values, the curve takes on an "L" shape. The flat part of the L-curve corresponds to the solution dominated by regularization errors, whereas the vertical part indicates that the solution is dominated by data errors. The optimal value of λ is at the corner of the curve where the curvature is at its maximum; this value marks the optimal balance between minimizing the regularization and data errors in the solution.

E. Optimization by SA

The object function of the proposed SRM model in (4) is nonconvex, and the solution is a categorical field. Because of these specifications, conventional optimization algorithms cannot be used to solve the proposed model. Furthermore, the SRM problem is characterized by a large solution space, which expands with land cover classes, the zoom factor, and image size. Therefore, to solve the problem within a reasonable computational time, we use the simulated annealing (SA) algorithm, which has been proposed to solve various global optimization problems, including the SRM problem [22], [36], [46], [52], [54].

Using the SA algorithm, we iteratively change the land cover class labels of subpixels to minimize the object function value in (4). The approach in [36] is adopted in this paper. The annealing schedule is based on a power law decay function, where temperature T_n at iteration n is changed to

$$T_n = \sigma \cdot T_{n-1}. \quad (10)$$

Parameter $\sigma \in (0, 1)$ controls the decrease rate of temperature T_n. In the initialization step, all the subpixels in each coarse pixel are randomly labeled according to the number of each class calculated by fraction images. For each iteration, all the subpixel labels are updated using a rowwise visiting scheme. The land cover class label of a subpixel is changed if doing so can decrease the object function value in (4). If this change increases the object function value, then this change will be accepted with a low probability according to the current temperature. The algorithm terminates when the minimum value of the object function is obtained, i.e., the previously fixed number of iterations is achieved or less than 0.1% of the subpixel labels are changed across three iterations.

The entire flowchart of the proposed model is shown in Fig. 1.

III. Experiments and Results

A. Synthetic Landsat Images

1) Data Description: In this experiment, the performance of the proposed SRM model is validated using synthetic multispectral images. The study area is located in the Brazilian Amazon Basin. A Landsat Enhanced Thematic Mapper (ETM+) scene acquired on July 18, 2005 is used. The original Landsat ETM+ image used for analysis includes bands 1, 2, 3, 4, 5, and 7. The experiment is conducted with a subset of 450 $\times$ 450 pixels, as shown in Fig. 2(a). The original Landsat ETM+ image is degraded to simulate coarse-resolution multispectral images. For a certain zoom factor, the digital number (DN)

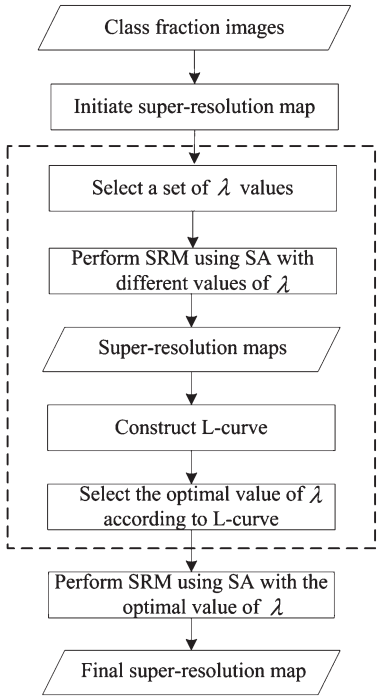

Fig. 1. Flowchart of the proposed SRM model.

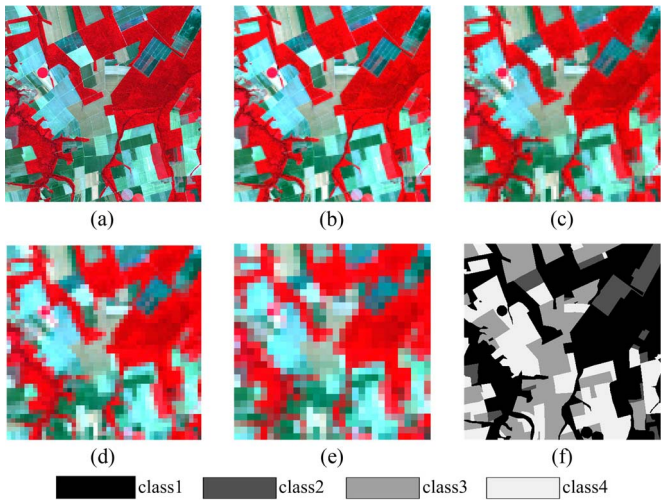

Fig. 2. (a) Landsat ETM+ multispectral image (band 4-3-2). (b)–(e) Degraded Landsat ETM+ images with zoom factor $z = 3$, 6, 10, and 15. (f) Reference land cover map digitized from (a).

values of the coarse-resolution pixel simulated for all the bands are the average DN values of the corresponding original Landsat ETM+ pixels. Four zoom factors, $z = 3$, $z = 6$, $z = 10$, and $z = 15$, are used in the experiment. Accordingly, the simulated coarse-resolution multispectral images are of 150 × 150 pixels with a resolution of 90 m, 75 × 75 pixels with a resolution of 180 m, 45 × 45 pixels with a resolution of 300 m, and 30 × 30 pixels with a resolution of 450 m [see Fig. 2(b)–(e)]. The SRM model was used to generate land cover maps with 450 × 450 pixels and a resolution of 30 m from the aforementioned simulated coarse-resolution multispectral images. To assess the performance of the proposed SRM model, we manually digitize the original Landsat ETM+ image, generating a reference fine-resolution land cover map, which comprises four land cover classes [see Fig. 2(f)]. The accuracy of the reference map is evaluated by using 200 ground sites extracted from a Google Earth image of the study area. The overall accuracy of the reference map is 96.5%.

2) Model Comparison and Validation: The SRM model that uses the L1 norm as the data fidelity term (L1_SRM) and the SRM model using the L2 norm as the data fidelity term (L2_SRM) are both used in this experiment. These proposed SRM models are compared with existing models for validation. The first model used for comparison is the maximal likelihood classification (MLC) model, a popular pixel-based hard classification model. The other three SRM models used for comparison are the MRF-based SRM model (MRF_SRM) [52], pixel-swapping-based SRM model (PS_SRM) [23], and HNN-based SRM model (HNN_SRM) [7]. Among these, MRF_SRM is directly applied to original coarse-resolution multispectral images. PS_SRM uses the fraction images generated by spectral unmixing as input and keeps class fractions unchanged. HNN_SRM uses the fraction images as input, and the constraints imposed by class fractions are relaxed.

The performance of all these models is visually and quantitatively assessed on the basis of the reference fine-resolution land cover map. The quality of the superresolution land cover maps produced by various models is assessed using the Kappa value, defined at the fine-resolution pixel level. We also use the root-mean-square error (RMSE) to compare the class area proportions in the resultant superresolution land cover map with those in the reference land cover map. The RMSE of the cth land cover class $RMSE_c$ is calculated as follows:

$$RMSE_c = \sqrt{\frac{1}{M_1 \times M_2} \sum_{V=1}^{M_1 \times M_2} \left(y^c_{V,SRM} - y^c_{V,REF} \right)^2} \tag{11}$$

where $y^c_{V,SRM}$ denotes the fraction value of the cth class in the coarse-resolution pixel V in the resultant superresolution land cover map and $y^c_{V,REF}$ denotes the fraction value of the cth class in the coarse-resolution pixel V in the reference land cover map.

3) Fraction Image Generation: Among all the aforementioned algorithms, MLC and MRF_SRM are directly applied to the multispectral image, whereas fraction images are used as input for L1_SRM, L2_SRM, PS_SRM, and HNN_SRM. Therefore, the fraction images must be produced by spectral unmixing before these SRM models are applied. To compare the effects of different fraction images on the results, two widely used spectral unmixing models are applied: the linear spectral mixture analysis (LSMA) model [59] and the multiple endmember spectral mixture analysis (MESMA) model [60].

In LSMA, the spectrum of the image pixels is determined by the sum of each endmember spectrum multiplied by its area percentage. Using the original Landsat ETM+ image, we directly obtain the endmember spectra in the simulated coarse-resolution multispectral images from the pixels dominated by an endmember land cover class. For each land cover class, 50 image spectra (pixels) are individually obtained. The average spectra are considered endmember spectra and used for spectral unmixing. Although LSMA is widely used in various

TABLE I
FRACTION RMSE VALUES OF LSMA AND MESMA FOR SYNTHETIC LANDSAT ETM+ IMAGES AT DIFFERENT ZOOM FACTORS

	LSMA					MESMA				
	Class1	Class2	Class3	Class4	Mean	Class1	Class2	Class3	Class4	Mean
$z = 3$	0.2271	0.2714	0.3529	0.3288	0.2951	0.2183	0.1989	0.2781	0.2641	0.2398
$z = 6$	0.2045	0.2836	0.3711	0.3434	0.3006	0.2105	0.1997	0.2726	0.2594	0.2355
$z = 10$	0.2051	0.2802	0.3554	0.3366	0.2943	0.1900	0.2043	0.2363	0.2500	0.2202
$z = 15$	0.2028	0.2810	0.3422	0.3221	0.2870	0.1966	0.2081	0.2586	0.2582	0.2304

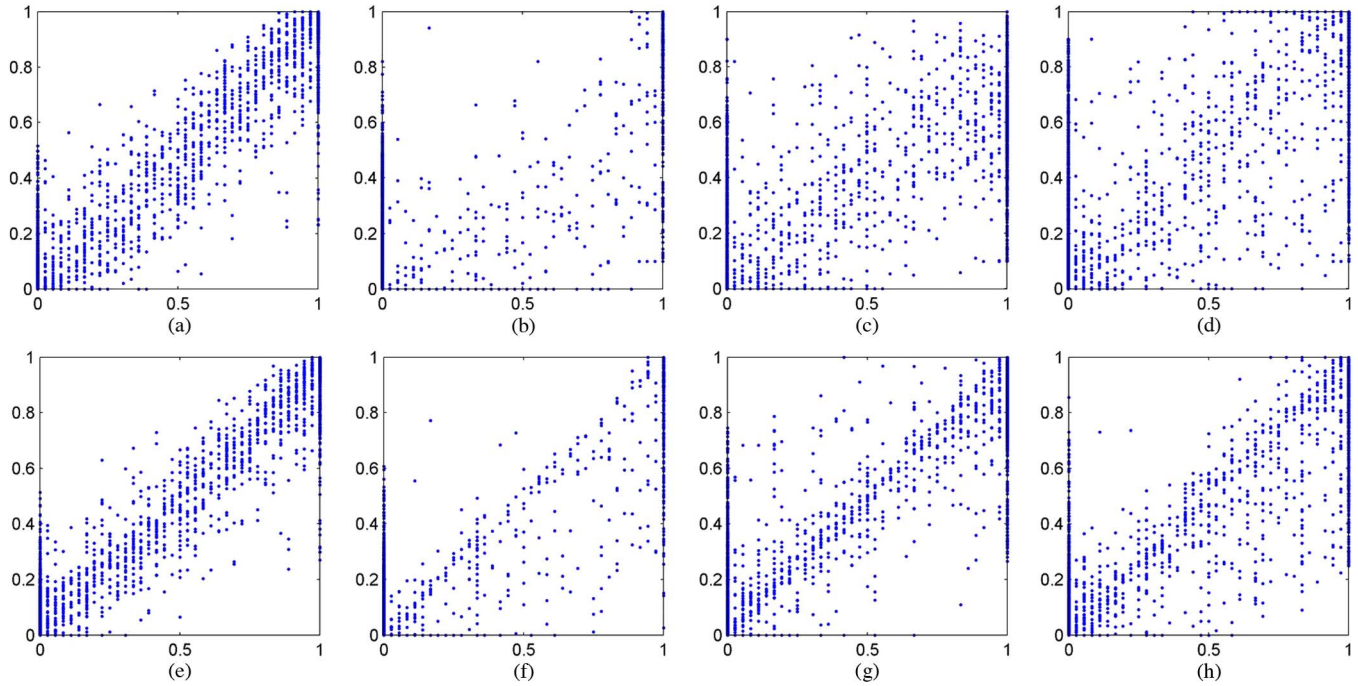

Fig. 3. Scatter plots of class area proportions from experiments at $z = 6$. The horizontal axis represents reference class proportions. The vertical axis represents class fractions produced by (a)–(d) LSMA and (e)–(h) MESMA (left to right, classes 1–4).

applications for different landscapes, it fails to account for spectral variations in the same land cover class because it uses fixed endmembers for all the pixels in an image.

MESMA is an extension of LSMA, enabling endmembers to vary on a pixel basis and represent more accurate spectral variability. By evaluating and selecting the best combination of endmember spectra from all possible combinations for each pixel, MESMA can precisely estimate land cover fraction. In this experiment, we use the average endmember RMSE to choose the optimal endmember spectra for each land cover class from selected image spectra [60]. Using the optimal endmembers, two-endmember, three-endmember, and four-endmember unmixing models are used, and the model with the smallest error is chosen for generating the final fraction images.

Table I shows the RMSEs of the fraction images derived using different spectral unmixing models. The zoom factor exerts no significant effect on spectral unmixing. With LSMA, class 1 has the lowest RMSE, whereas classes 3 and 4 have the highest. With MESMA, class 2 has the lowest RMSE, and classes 3 and 4 exhibit a decreased RMSE of about 0.08. Therefore, the mean RMSE of LSMA is about 0.3 for all zoom factors, and that of MESMA is about 0.23, suggesting that MESMA is superior to LSMA.

The scatter plots (see Fig. 3) of the land cover fractions of the reference fine-resolution map and those produced by LSMA and MESMA at $z = 6$ show that dispersion with LSMA is larger than that with MESMA. The fraction error histograms that correspond to the scatter plots shown in Fig. 4 reveal that the error histograms of different land cover classes vary with spectral unmixing models. Visually, the error histogram of class 1 [see Fig. 4(a)] is close to a normal distribution when LSMA is used. The error histogram of class 3 has a bimodal distribution, whereas that of class 4 has a significant tailed distribution on the right portion. When MESMA is used, however, the bimodal distribution of class 3 and the tailed distribution of class 4 disappear. All the error histograms are close to a normal distribution.

4) L-Curve Method: In this section, the method for determining the value of λ with the L-curve criterion is validated. The L1_SRM or L2_SRM model with different values of λ

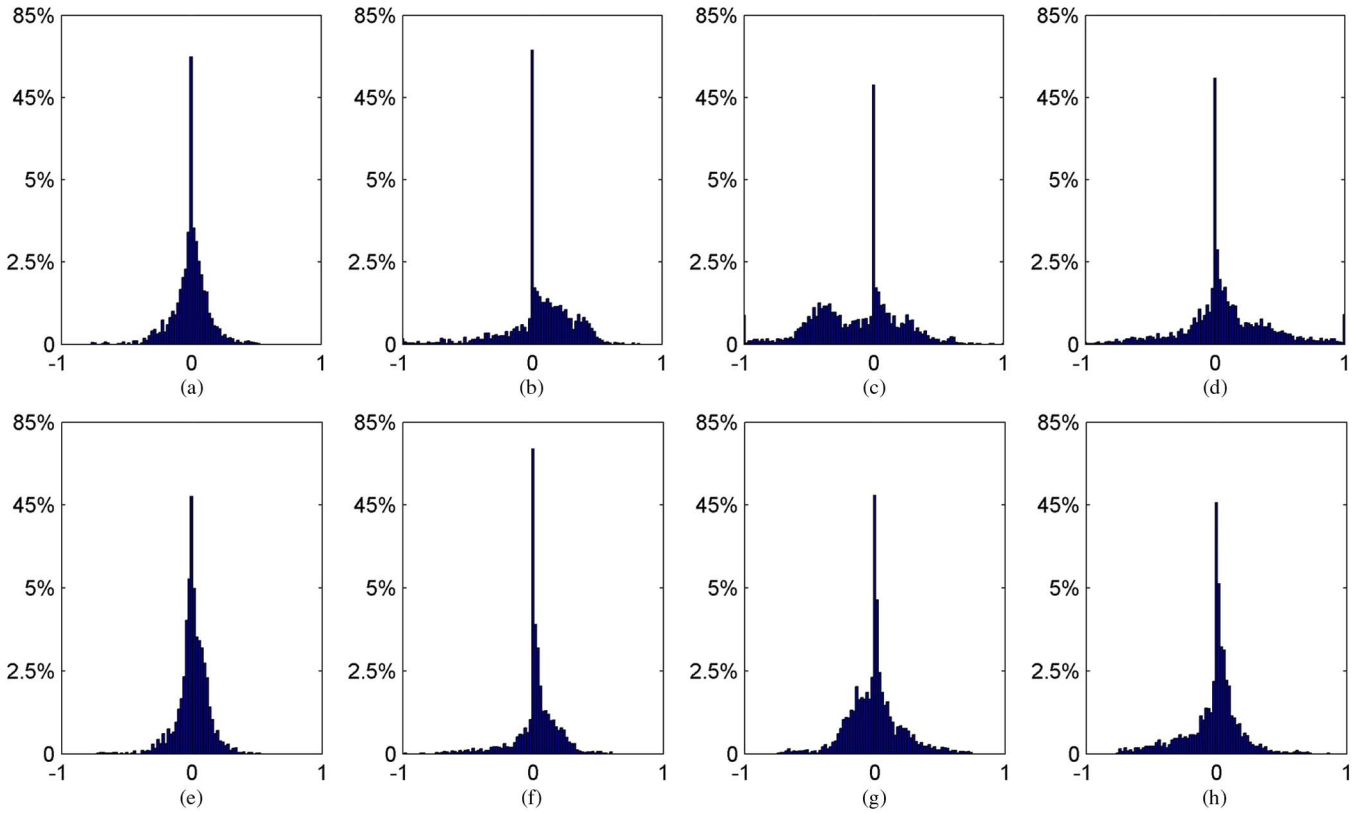

Fig. 4. Histograms of class proportion errors at $z = 6$ for (a)–(d) LMSA and (e)–(h) MESMA (left to right, classes 1–4).

is first used to generate the superresolution land cover map. The values of $D(X, Y, H)$ and $R(X)$, which are the residual fraction error and solution smoothness for each superresolution land cover map, respectively, are then calculated and plotted on a log-log scale. A cubic smoothing spline curve is fitted as the L-curve by using the plotted points. Finally, the curvature of the fitted curve is calculated, and the maximal curvature value is considered the corner.

Fig. 5 shows the representative samples of the L-curve at $z = 6$ for both L1_SRM and L2_SRM models, which use the fraction images estimated by LSMA and MESMA. The points of $D(X, Y, H)$ and $R(X)$, as well as the fitted cubic smoothing spline curve, are shown on the top line of Fig. 5. The calculated curvature that corresponds to the fitted spline curve is shown on the middle line. On the bottom line, the Kappa coefficients of the final superresolution land cover map for each value of λ are accordingly plotted. In all the images, the "L" shape of the fitted curve is noticeable, although the shapes themselves differ. The low value of λ represents the vertical part in the L-curve, where $D(X, Y, H)$ is low and $R(X)$ is high. Therefore, the final superresolution land cover map is dominated by the data fidelity term. The increase in λ increases $D(X, Y, H)$ and decreases $R(X)$. Therefore, the spatial regularization term increasingly influences the final superresolution land cover map. Accordingly, the flat part of the L-curve corresponds to a solution with a high value of λ dominated by fraction errors. On the basis of the L-curve criterion, the optimal value of λ is found at the corner where the curvature is at its maximum.

A similar trend illustrated by the L-curve exists in the relationship between the Kappa and the λ values. The Kappa value is also low when λ is low because the SRM solution is characterized by considerable noise. The increase in λ also increases the Kappa value because of the elimination of noise in the SRM solution. Once the Kappa reaches its maximal value, it begins to decrease with increasing λ because of the oversmoothed result. For all the images in this experiment, the maximal values of the calculated curvature of the L-curve correspond to the maximal Kappa values. Although not the highest, the Kappa values of the final superresolution land cover maps generated with the values of λ chosen by using the L-curve criterion are desirable, verifying the validity of the L-curve criterion in identifying the regularization parameter.

5) Model Parameters: The zoom factor considerably affects the performance of the proposed SRM models (see Table II). With the increment in z, the spatial location of subpixels tends to be incorrect, particularly under a larger zoom factor. Kappa values decrease by about 0.01, 0.02, and 0.04 when z increases from 3 to 6, 6 to 10, and 10 to 15, respectively, for L1_SRM and L2_SRM which use LSMA fraction images. The Kappa values decrease by 0.02, 0.03, and 0.07 when z increases from 3 to 6, 6 to 10, and 10 to 15, respectively, for the models that use MESMA fraction images.

The spectral unmixing model generates the input of L1_SRM and L2_SRM, thereby influencing SRM performance. Kappa values more significantly improve for MESMA than for LSMA, with the models having different values of z, w, and κ (see Table II). At a z smaller than 15, the increments in Kappa values of L1_SRM and L2_SRM that use MESMA fraction images are higher than 0.1 compared with the Kappa values of the models that use LSMA fraction images. At a small z,

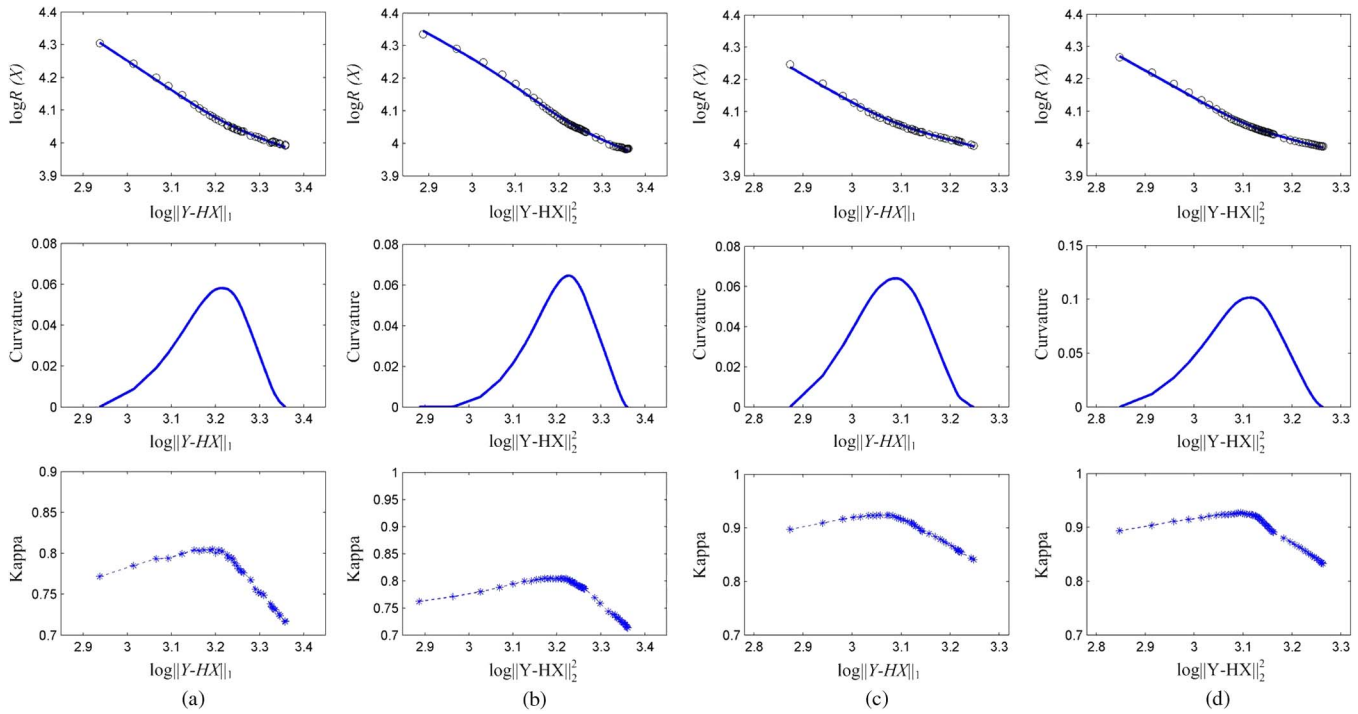

Fig. 5. L-curves, curvatures, and Kappa values of the degraded Landsat ETM+ image at $z = 6$. (a) L1_SRM that uses LSMA fraction images. (b) L2_SRM that uses LSMA fraction images. (c) L1_SRM that uses MESMA fraction images. (d) L2_SRM that uses MESMA fraction images.

the accuracy of SRM more strongly depends on the fraction images. By contrast, at a large z, the accuracy of SRM depends to a relatively less extent on the fraction images because the spatial location of subpixels is hard to be mapped correctly, resulting in relatively unsustainable mapping accuracy.

The Kappa values of L2_SRM (see Table II) are relatively higher than those of L1_SRM in most cases because the error distributions of the fraction images are closer to a normal distribution (see Fig. 4). The L2 norm used in L2_SRM generally performs better for Gaussian noise, whereas the L1 norm used in L1_SRM performs better for Laplacian noise. Given the same fraction images and model parameters, however, the differences between L2_SRM and L1_SRM are minimal, and the Kappa values of L2_SRM are only about 0.005 higher than those of L1_SRM. Moreover, the optimal λ values in L2_SRM are lower than those in L1_SRM because the class fraction residual vector has a range of $[-1, 1]$, generating an L2 norm residual vector that is smaller than the L1 norm residual vector.

The value of w influences the number of subpixels considered in the computation of the regularization term. More subpixels are therefore introduced to influence the regularization term of a particular subpixel with the increment in w. Table II shows that the Kappa values are low when $w = 3$ because only the eight nearest neighboring subpixels that are spatially correlated within a small range affect the regularization term calculation for a target subpixel. In this case, the resultant superresolution land cover map is usually unsmoothed. By contrast, when $w > 3$, the Kappa values of the superresolution land cover maps generated by L1_SRM and L2_SRM are similar and higher than those of the land cover maps generated when $w = 3$.

Nonlinear parameter κ affects the influence of spatially neighboring subpixels on the central subpixel with respect to geometric distance. A high κ assigns low weights to spatially neighboring subpixels that are geometrically distant from a target subpixel. The optimal value of κ is related to the value of w, and the Kappa values are low for different values of κ when $w = 3$ (see Table II). When $w > 3$, a low value of κ in L1_SRM or L2_SRM can usually generate superresolution land cover maps with high Kappa values. Moreover, in most cases, the optimal values of λ tend to increase with the increment in κ for both L1_SRM and L2_SRM.

6) Comparison With Other Algorithms: Fig. 6 $(z = 6)$ shows the resultant superresolution land cover maps generated by MLC and MRF_SRM, which are directly applied to the coarse-resolution image, as well as L1_SRM, L2_SRM, PS_SRM, and HNN_SRM, which are applied to the fraction images produced by LSMA and MESMA. MLC generates a pixel-based land cover map with jagged boundaries and missed the detailed spatial information on land cover [see Fig. 6(a)]. MRF_SRM generates a superresolution land cover map with smooth boundaries. However, many corners of the land cover boundaries are round, and the shapes of many patches are incorrectly mapped [see Fig. 6(f)]. The superresolution land cover maps produced by PS_SRM are characterized by many speckle artifacts because of the fraction errors caused by spectral unmixing [see Fig. 6(b) and (g)]. HNN_SRM decreases speckle artifacts, especially by using the fraction images produced by MESMA, whose fraction error is less severe [see Fig. 6(c) and (h)]. By contrast, the superresolution land cover maps produced by L1_SRM and L2_SRM are similar to the reference because more speckle artifacts are eliminated and the shape boundaries are well retained [see Fig. 6(d), (e), (i), and (j)]. Using MESMA fraction images instead of LSMA fraction images as input can produce better superresolution land cover maps for both

TABLE II
KAPPA VALUES AND FRACTION RMSE VALUES OF L1_SRM AND L2_SRM USING FRACTION IMAGES PRODUCED BY LSMA AND MESMA AS INPUT, FOR SYNTHETIC LANDSAT ETM+ IMAGES AT DIFFERENT ZOOM FACTORS

			L1_SRM						L2_SRM					
			κ=0		κ=1		κ=2		κ=0		κ=1		κ=2	
			λ	Kappa	λ	Kappa	λ	Kappa	λ	Kappa	λ	Kappa	λ	Kappa
z=3	LMSA	w=3	0.51	0.8050	0.55	0.8052	0.85	0.8040	0.42	0.8058	0.40	0.8050	0.60	0.8062
		w =5	0.50	0.8126	0.62	0.8105	0.65	0.8118	0.30	0.8149	0.35	0.8129	0.40	0.8141
		w =7	0.35	0.8122	0.42	0.8136	0.60	0.8139	0.25	0.8145	0.25	0.8156	0.32	0.8168
		w =9	0.25	0.8112	0.30	0.8123	0.42	0.8130	0.21	0.8137	0.20	0.8155	0.25	0.8161
	MESMA	w =3	0.55	0.9444	0.60	0.9444	0.70	0.9439	0.50	0.9445	0.50	0.9437	0.51	0.9437
		w =5	0.35	0.9454	0.42	0.9464	0.52	0.9470	0.19	0.9461	0.25	0.9467	0.25	0.9464
		w =7	0.40	0.9403	0.40	0.9451	0.50	0.5000	0.17	0.9438	0.18	0.9464	0.20	0.9472
		w =9	0.33	0.9401	0.33	0.9443	0.40	0.9476	0.15	0.9433	0.17	0.9462	0.18	0.9450
z=6	LMSA	w =3	0.24	0.7849	0.50	0.7866	0.51	0.7861	0.15	0.7888	0.35	0.7906	0.17	0.7903
		w =5	0.22	0.8011	0.22	0.8008	0.26	0.8022	0.095	0.8029	0.13	0.8041	0.17	0.8050
		w =7	0.14	0.8037	0.17	0.8050	0.20	0.8038	0.064	0.8049	0.065	0.8048	0.12	0.8044
		w =9	0.11	0.8041	0.13	0.8071	0.15	0.8035	0.055	0.8046	0.065	0.8068	0.095	0.8072
	MESMA	w =3	0.29	0.9109	0.27	0.9110	0.30	0.9104	0.11	0.9137	0.11	0.9132	0.15	0.9135
		w =5	0.14	0.9202	0.14	0.9193	0.18	0.9173	0.055	0.9218	0.065	0.9211	0.094	0.9204
		w =7	0.12	0.9207	0.12	0.9229	0.14	0.9212	0.055	0.9231	0.055	0.9237	0.075	0.9226
		w =9	0.10	0.9185	0.11	0.9228	0.12	0.9228	0.045	0.9227	0.045	0.9233	0.060	0.9230
z=10	LMSA	w =3	0.92	0.7522	0.28	0.7587	0.22	0.7572	0.035	0.7578	0.069	0.7636	0.060	0.7623
		w =5	0.076	0.7826	0.082	0.7768	0.081	0.7753	0.033	0.7895	0.039	0.7850	0.045	0.7840
		w =7	0.065	0.7829	0.064	0.7826	0.08	0.7815	0.032	0.7924	0.027	0.7913	0.039	0.7876
		w =9	0.052	0.7813	0.062	0.7814	0.063	0.7833	0.018	0.7937	0.021	0.7910	0.027	0.7912
	MESMA	w =3	0.21	0.8754	0.24	0.8750	0.50	0.8740	0.042	0.8749	0.052	0.8758	0.057	0.8753
		w =5	0.062	0.8889	0.090	0.8863	0.095	0.8836	0.033	0.8943	0.021	0.8920	0.024	0.8885
		w =7	0.055	0.8990	0.053	0.8937	0.071	0.8878	0.024	0.8975	0.021	0.8948	0.024	0.8922
		w =9	0.053	0.8915	0.056	0.8985	0.057	0.8920	0.018	0.8982	0.018	0.8978	0.021	0.8948
z=15	LMSA	w =3	0.11	0.6768	0.11	0.6852	0.16	0.6816	0.022	0.6767	0.025	0.6860	0.025	0.6798
		w =5	0.057	0.7342	0.074	0.7371	0.12	0.7313	0.022	0.7433	0.025	0.7374	0.025	0.7405
		w =7	0.043	0.7473	0.055	0.7422	0.053	0.7352	0.015	0.7483	0.015	0.7468	0.015	0.7436
		w =9	0.035	0.7475	0.032	0.7469	0.042	0.7431	0.015	0.7551	0.015	0.7525	0.015	0.7470
	MESMA	w =3	0.043	0.7630	0.097	0.7661	0.10	0.7659	0.025	0.7632	0.035	0.7669	0.015	0.7657
		w =5	0.046	0.8094	0.040	0.8009	0.086	0.8022	0.012	0.8142	0.012	0.8120	0.015	0.8079
		w =7	0.031	0.8204	0.033	0.8139	0.057	0.8042	0.012	0.8262	0.012	0.8238	0.011	0.8143
		w =9	0.033	0.8225	0.031	0.8161	0.033	0.8104	0.012	0.8256	0.012	0.8260	0.012	0.8183

L1_SRM and L2_SRM. No obvious difference exists between the superresolution land cover maps generated by L1_SRM and L2_SRM when the same fraction images are used as input.

The Kappa values and fraction RMSE values of the different models are shown in Table III, which indicates that all the accuracy levels are affected by the zoom factor. With the increment in z, Kappa values tend to decrease, and fraction RMSE values tend to increase. For a given z, the Kappa values of SRM are usually higher than those of MLC, and the fraction RMSE values of SRM are usually lower than those of MLC. Among the SRM algorithms that use LSMA fraction images as input, PS_SRM exhibits the lowest Kappa values. The Kappa values of HNN_SRM are higher than those of PS_SRM because HNN_SRM can eliminate fraction errors to a certain extent. L1_SRM and L2_SRM generate superresolution land cover maps with Kappa values and fraction RMSE values that are higher and lower, respectively, than those of the superresolution land cover maps generated by PS_SRM and HNN_SRM. This difference indicates the effectiveness of the proposed model in reducing fraction errors. The Kappa values and fraction RMSE

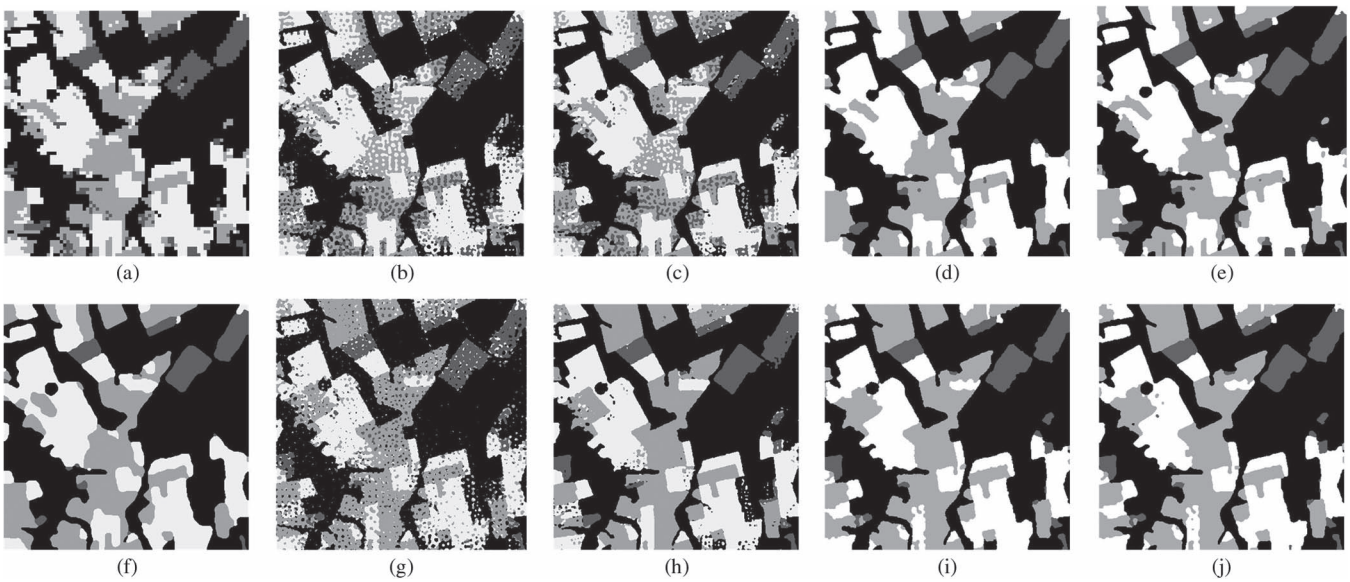

Fig. 6. Land cover maps generated from degraded Landsat ETM+ image at $z = 6$ by (a) MLC and (f) MRF_SRM. Land cover maps generated by (b) PS_SRM, (c) HNN_SRM, (d) L1_SRM, and (e) L2_SRM that use LSMA fraction images. Land cover maps generated by (g) PS_SRM, (h) HNN_SRM, (i) L1_SRM, and (j) L2_SRM that use MESMA fraction images.

TABLE III
KAPPA VALUES AND FRACTION RMSE VALUES OF DIFFERENT MODELS, FOR SYNTHETIC LANDSAT ETM+ IMAGES AT DIFFERENT ZOOM FACTORS

				LMSA				MESMA			
		MLC	MRF_SRM	PS_SRM	HNN_SRM	L1_SRM	L2_SRM	PS_SRM	HNN_SRM	L1_SRM	L2_SRM
z=3	Kappa	0.7715	0.8603	0.7088	0.8055	0.8125	0.8148	0.8276	0.9445	0.9453	0.9460
	RMSE	0.2713	0.2143	0.3046	0.2468	0.2418	0.2404	0.2358	0.1330	0.1291	0.1312
z=6	Kappa	0.7717	0.8041	0.7040	0.7408	0.8010	0.8028	0.8117	0.9187	0.9201	0.9217
	RMSE	0.2725	0.2482	0.3007	0.2822	0.2495	0.2479	0.2353	0.1276	0.1537	0.1543
z=10	Kappa	0.7508	0.8024	0.6861	0.7532	0.7825	0.7895	0.8008	0.8763	0.8889	0.8943
	RMSE	0.2855	0.2467	0.2943	0.2670	0.2556	0.2520	0.2202	0.1749	0.1685	0.1708
z=15	Kappa	0.7102	0.7549	0.6232	0.6774	0.7342	0.7432	0.6866	0.7637	0.8093	0.8142
	RMSE	0.3077	0.2663	0.2870	0.2799	0.2718	0.2691	0.2303	0.2133	0.2179	0.2140

values of L1_SRM and L2_SRM, which use LSMA fraction images, are slightly worse than those of MRF_SRM because the LSMA fraction images are characterize by excessively large errors. By contrast, using MESMA fraction images as input improves L1_SRM and L2_SRM. The Kappa values increase by about 0.1 and exceed those of MRF_SRM. The fraction RMSE values decrease by about 0.1 and become lower than those of MRF_SRM. Therefore, the proposed model is more flexible than MRF_SRM because the former allows for the selection of more accurate fraction images as input.

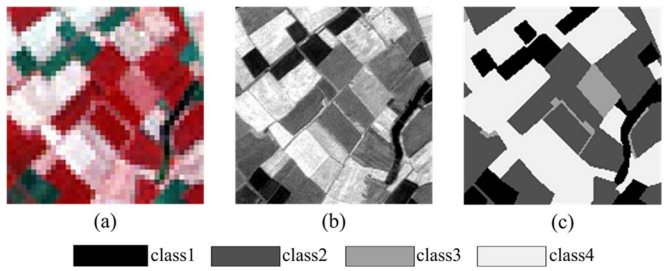

Fig. 7. (a) IKONOS multispectral image (band 4-3-2). (b) IKONOS panchromatic image. (c) Reference land cover map digitized from the panchromatic image.

B. Real IKONOS Images

The performance of the proposed model in addressing a real natural phenomenon is assessed using an IKONOS image to provide a more realistic test. The test area is a farmland located at nearby Dujiangyan City, Sichuan Province, China. The experiment is conducted using a real multispectral IKONOS image with 40×40 pixels (at 4-m spatial resolution), as shown in Fig. 7(a). A reference fine-resolution thematic map (at 1-m spatial resolution) was generated by manually digitizing the corresponding panchromatic band of the image shown in Fig. 7(b). The reference land cover map comprises four crisp land cover classes [see Fig. 7(c)]. We evaluate the accuracy of the reference map by using 120 ground sites extracted from a Google Earth image of the study area. The overall accuracy of the reference map is 94.2%. Similar to the synthetic Landsat image experiment, endmembers are manually chosen in the

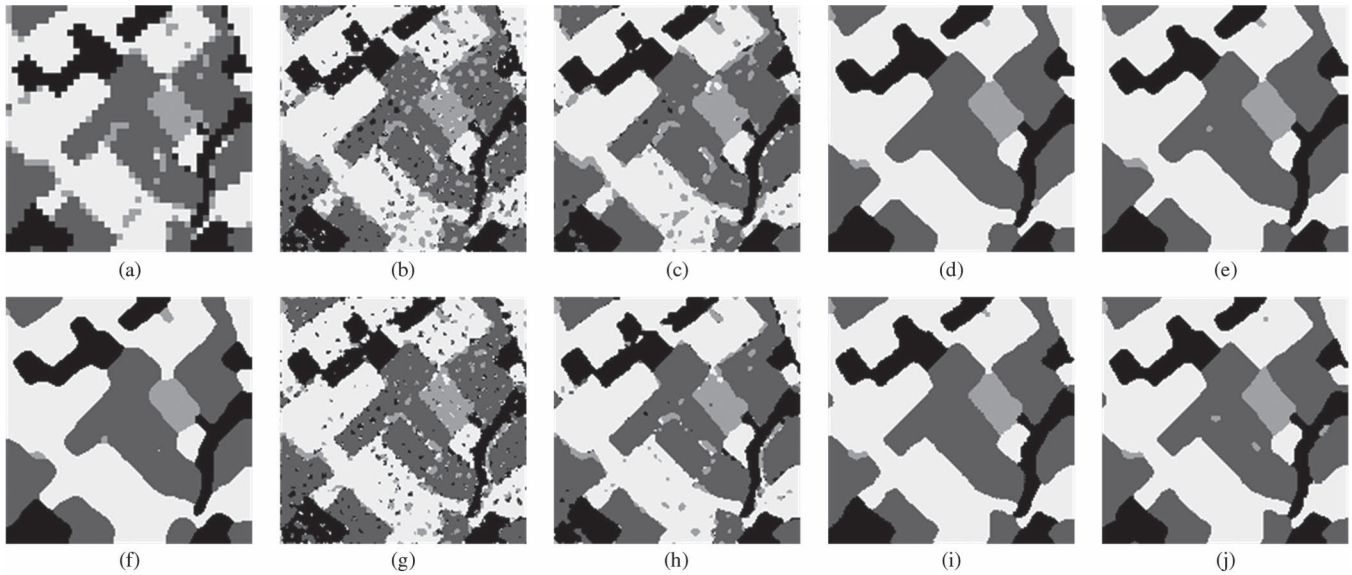

Fig. 8. Land cover maps generated from IKONOS image by (a) MLC and (f) MRF_SRM. Land cover maps generated by (b) PS_SRM, (c) HNN_SRM, (d) L1_SRM, and (e) L2_SRM that use LSMA fraction images. Land cover maps generated by (g) PS_SRM, (h) HNN_SRM, (i) L1_SRM, and (j) L2_SRM that use MESMA fraction images.

TABLE IV
KAPPA VALUES AND FRACTION RMSE VALUES OF DIFFERENT MODELS FOR THE IKONOS IMAGE

			LMSA				MESME			
	MLC	MRF_SRM	PS_SRM	HNN_SRM	L1_SRM	L2_SRM	PS_SRM	HNN_SRM	L1_SRM	L2_SRM
Kappa	0.8076	0.8699	0.7149	0.7920	0.8750	0.8798	0.7858	0.8620	0.8964	0.9001
RMSE	0.2523	0.1987	0.3028	0.2576	0.1961	0.1909	0.2561	0.2039	0.1779	0.1732

original 4-m spatial resolution image, and LSMA and MESMA are used to generate fraction images. Using the fraction images as input, L1_SRM and L2_SRM models are applied to generate the final superresolution land cover map. The value of λ is selected with the aforementioned L-curve criterion. The parameters of all the models are the same as those in the experiment on the synthetic Landsat ETM+ images.

The final land cover maps of MLC, together with the results of MRF_SRM, PS_SRM, HNN_SRM, L1_SRM, and L2_SRM, are displayed in Fig. 8. Similar to the results on the degraded Landsat ETM+ images, the resultant land cover map generated by MLC has jagged boundaries, whereas the superresolution land cover map generated by MRF_SRM has smooth boundaries. Many speckle artifacts exist in the superresolution land cover map generated by PS_SRM; HNN_SRM reduces these speckle artifacts, most of which are eliminated by L1_SRM and L2_SRM. The SRM models that use MESMA fraction images show visible improvement over those that use LSMA fraction images. However, many linear features disappear in the results of L1_SRM and L2_SRM because of the spatial regularization model, which favors a more homogeneous land cover map over isolated pixels. This preference results in the loss of some small targets of interest.

The accuracy measures of all the approaches are shown in Table IV. The Kappa values of PS_SRM are lower than those of MLC, and the fraction RMSE values of PS_SRM are higher than those of MLC. When MLC is applied, all the subpixels in the mixed pixels are assigned to the land cover class with the highest area percentage. Consequently, some small area land cover classes are overlooked, but the largest area land cover class in the mixed pixel is correctly mapped. However, when the PS_SRM model is applied, parts of the largest area land cover class in the mixed pixels are incorrectly mapped as other land cover classes because of the spectral unmixing error. As a result, a less precise superresolution land cover map is produced. For other SRM models, most speckle artifact areas disappear because of the spatial smoothing effect of MRF_SRM and the spatial regularization implemented with L1_SRM and L2_SRM. Thus, the Kappa values of MRF_SRM, L1_SRM, and L2_SRM (LSMA fraction images) are similarly high. Moreover, the Kappa values increase and the fraction RMSE values decrease for all the SRM models when MESMA fraction images are used as input.

C. Real Hyperspectral Images

The performance of the proposed model is also tested on a real hyperspectral Airborne Visible/Infrared Imaging Spectrometer (AVIRIS) image. The AVIRIS image includes 224 bands (spectral range of 0.4–2.4 μm) with a spatial resolution of 17 m. The experiment is conducted using a subset of 180 $\times$ 70 pixel AVIRIS images of an airport located in Moffett Field, San Francisco Bay [see Fig. 9(a)]. The reference fine-resolution land cover map is produced by manual digitization using a

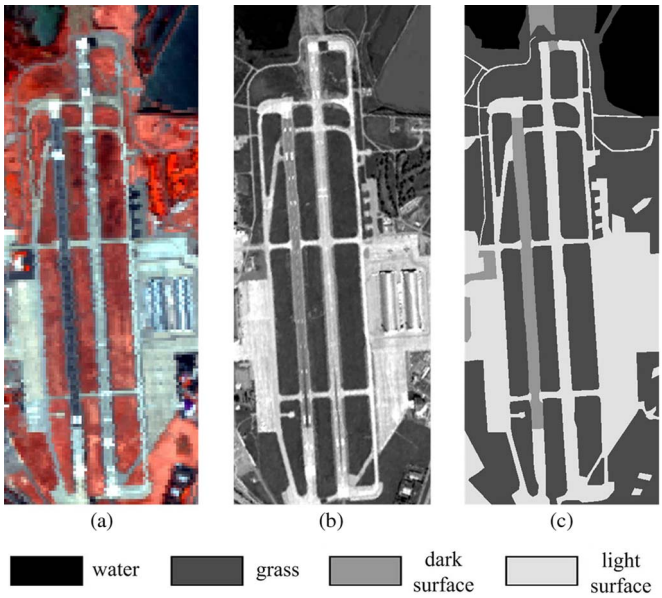

Fig. 9. (a) AVIRIS hyperspectral image (band 40-20-15). (b) Google Earth image. (c) Reference land cover map.

high-spatial-resolution Google Earth image of 900 × 350 pixels [see Fig. 9(b) and (c)]. The zoom factor is set to 5. Four land cover classes, namely, water, grass, dark surface, and white surface, appear on the images. The endmember signatures in the AVIRIS image are manually selected, and LSMA and MESMA are applied to generate fraction images. The values of λ in L1_SRM and L2_SRM are selected with the aforementioned L-curve criterion. The parameters of all the models are the same as those in the experiment on the synthetic Landsat ETM+ images.

The land cover maps produced by the MLC and SRM models are shown in Fig. 10. MLC generates a land cover map with gaggled boundaries, whereas the SRM models generate land cover maps with smooth boundaries. Unlike the land cover maps produced by the models that use LSMA fraction images, those produced by PS_SRM and HNN_SRM, which use MESMA fraction images, show fewer speckle artifacts. The land cover boundaries produced by L1_SRM and L2_SRM are straighter. However, most of the path objects located in the upper side of the scene are eliminated in the land cover maps produced by L1_SRM and L2_SRM. In general, the land cover maps produced by the SRM models that use MESMA fraction images more closely resemble the reference map than those produced by the SRM models that use LSMA fraction images.

The accuracy statistics of different models are shown in Table V. The Kappa value of MLC is low because of the mixed pixel problem. A substantial difference in Kappa values exists among various SRM models. In general, the Kappa values of the SRM model that uses MESMA fraction images are higher than the Kappa values of those that use LSMA fraction images. This result is attributed to the fraction RMSE of MESMA (0.2302), which is lower than that of LSMA (0.3276). In addition, the Kappa values of L1_SRM and L2_SRM are higher than those of PS_SRM and HNN_SRM because L1_SRM and L2_SRM can better eliminate speckle artifacts, showing the advantages of the proposed models.

D. Discussion

The theoretical and experimental results of this paper confirm that the accuracy of fraction images is important in SRM and that reducing fraction image errors increases SRM accuracy. In general, the fraction images generated by the MESMA unmixing model exhibit lower errors than those generated by the LSMA unmixing model. The SRM model that uses MESMA fraction images generates superresolution maps with accuracy levels that are higher than those generated by the models that use LSMA fraction images. This result supports the idea that high-accuracy fraction images can increase the accuracy of superresolution maps produced by SRM. The experimental results show that the regularization term in the proposed model can, to a certain extent, reduce fraction image errors by spatially smoothing land cover patches. However, a larger regularization parameter is often needed to reduce large fraction errors, causing more detailed land cover information to be simultaneously eliminated. Thus, selecting an optimal spectral unmixing model can minimize fraction image errors and increase the accuracy of SRM models that use fraction images as input. Although fraction image errors can rarely be avoided by spectral unmixing models [4], [5], we can select spectral unmixing models, such as nonlinear unmixing models, with the least fraction error as input to generate a superresolution map with the highest accuracy. Within those SRM models, MRF_SRM is directly applied on remotely sensed images by using spectral constraints, which is indeed the simple Gaussian spectral unmixing algorithm, instead of the proportion constraints provided by fraction images. The experimental results show that the proposed SRM model, which uses MESMA fraction images, generates superresolution maps with accuracy higher than that of the maps generated by MRF_SRM. Therefore, the proposed SRM models are flexible because different spectral unmixing algorithms can be used to produce land cover fraction images as SRM input.

In the experiments, the L1 and L2 norms are tested as the data fidelity terms. The accuracy of superresolution land cover maps varies with different norms. In general, the choice of the data fidelity term should correspond with the feature of noise included in the inputted fraction images, where the L2 norm is appropriate when noise distribution is Gaussian and the L1 norm is appropriate when noise distribution is Laplacian. In practice, adopting a mixed L1–L2 norm in the SRM data fidelity term should be more suitable because fraction image noises are often space-variable fusion errors of different distributions.

We use the maximal spatial dependence principle, which is identical to the smoothness principle, for spatial regularization. It is appropriate for smoothing a homogeneous region within which uniform land cover classes can be found. However, it is unsuitable in images with edges because it tends to oversmooth such edges. Edge-preserving regularization terms, such as anisotropic land cover dependence models [11], [14], can also be adopted in the regularization term of the proposed model to preserve edges and detailed information on land cover patches.

The regularization parameter has an important function in L1_SRM and L2_SRM; it is used to balance the contribution of the regularization and data fidelity terms. In this paper,

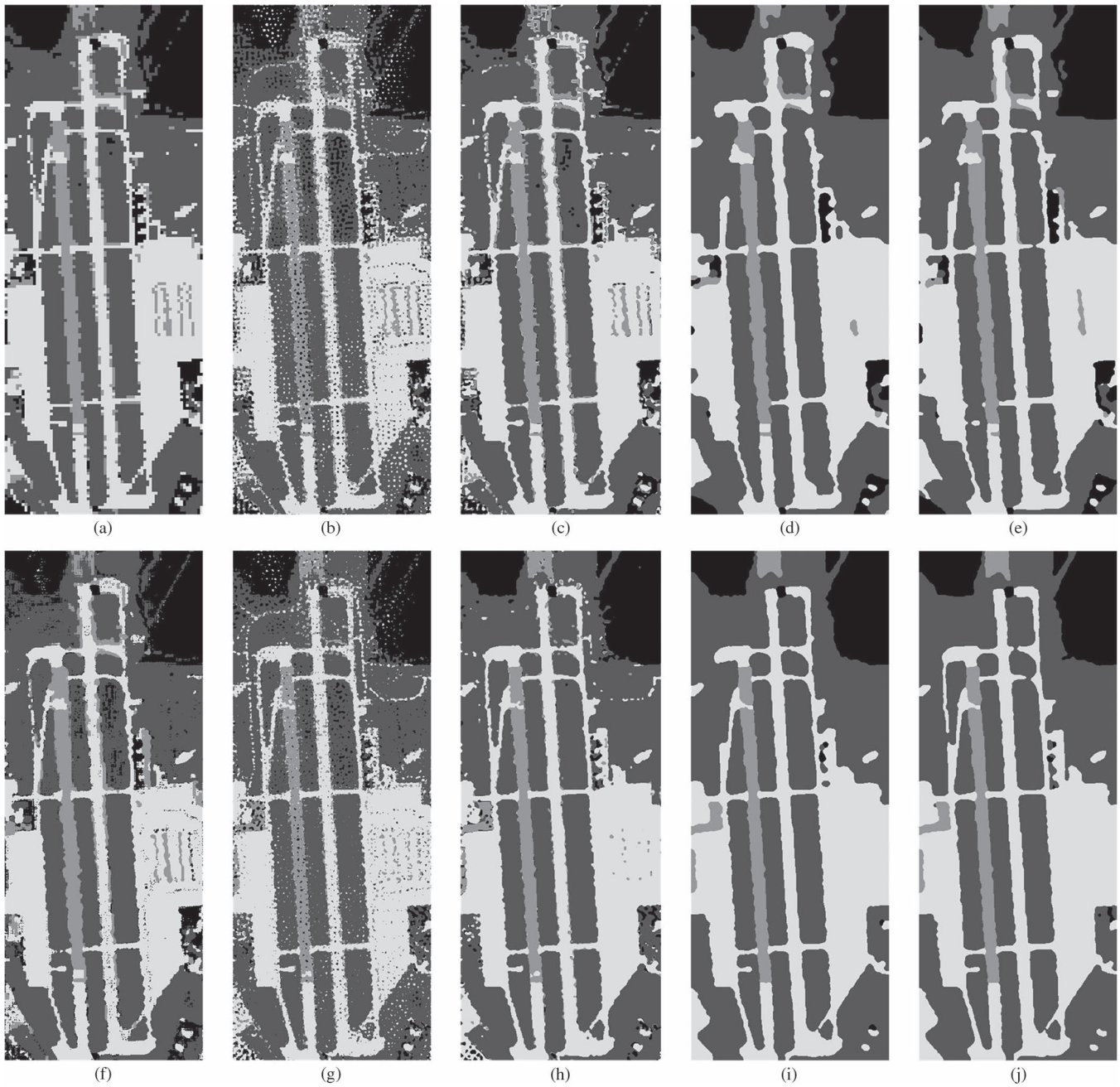

Fig. 10. Land cover maps generated from ARIVIS image by (a) MLC and (f) MRF_SRM. Land cover maps generated by (b) PS_SRM, (c) HNN_SRM, (d) L1_SRM, and (e) L2_SRM that use LSMA fraction images. Land cover maps generated by (g) PS_SRM, (h) HNN_SRM, (i) L1_SRM, and (j) L2_SRM that use MESMA fraction images.

TABLE V
KAPPA VALUES AND FRACTION RMSE VALUES OF DIFFERENT MODELS FOR THE AVIRIS IMAGE

			LMSA				MESME			
	MLC	MRF_SRM	PS_SRM	HNN_SRM	L1_SRM	L2_SRM	PS_SRM	HNN_SRM	L1_SRM	L2_SRM
Kappa	0.7367	0.7252	0.6383	0.7303	0.7935	0.7959	0.8084	0.8945	0.9249	0.9283
RMSE	0.2802	0.2863	0.3262	0.2808	0.2397	0.2381	0.2299	0.1700	0.1250	0.1324

the L-curve method is used to select the optimal value of the regularization parameter. Although the L-curve method effectively selects the optimal regularization parameter, it requires a set of superresolution land cover maps produced by L1_SRM (or L2_SRM) with different regularization parameter values. Other methods widely used for regularization should be further studied [51]. We adopt a fixed regularization parameter, which disregards local properties. Homogeneous regions typically often require a high-weight regularization parameter to remove speckle artifacts, whereas class boundaries require

TABLE VI
RUNNING TIME OF DIFFERENT SRM MODELS FOR DIFFERENT IMAGES

Image	Number of pixels	Number of bands	Number of classes	Zoom factor	MRF_SRM	PS_SRM	HNN_SRM	L1_SRM/ L2_SRM
Landsat	450×450	6	4	6	96min	30min	1567min	41min
IKONOS	160×160	4	4	4	8min	2min	102min	3min
AVIRIS	900×350	224	4	5	288min	24min	1960min	53min

a low-weight regularization parameter to maintain boundary shapes. Applying a spatially adaptive method for regularization parameter estimation can solve this problem [53].

Program run time influences the application of the SRM models. All the models are tested on an Intel Core 2 Processor 2.66-GHz Duo CPU with 1.98-GB RAM using MATLAB version 7.3. The iteration number is 120 for PS_SRM, MRF_SRM, L1_SRM, and L2_SRM and 4000 for HNN_SRM. The run times of different SRM models are listed in Table VI. Run time increases with image size and zoom factor for different SRM models. PS_SRM converges faster than the other SRM algorithms. The complexity of the MRF_SRM model is related to the number of bands and land cover classes, and its run time increases with the number of bands and land cover classes. For the PS_SRM, HNN_SRM, L1_SRM, and L2_SRM models that use fraction images as input, run time increases with the number of land cover classes. The run times of L1_SRM and L2_SRM are much shorter than those of MRF_SRM and HNN_SRM, demonstrating the advantages of the proposed models.

IV. CONCLUSION

This paper considers the superresolution land cover mapping problem from a new perspective based on regularization theory, which considers SRM an inversion problem. This new viewpoint aims to recover superresolution land cover maps from inputted fraction images by using an observation model that connects them and by exploiting *a priori* knowledge about the land cover maps. It is unlike the traditional models that consider SRM as an optimization problem, in which the spatial dependence is maximized as the goal and the fraction images are maintained as constraints. Considering SRM under the perspective of a regularization problem can relevantly be a unified approach to reconstructing final superresolution land cover maps. The proposed approach is also easy to implement and eliminates the errors caused by inputted fraction images.

Within the regularization framework, two SRM models are constructed by using spatial dependence as the regularization term and the L1 or L2 norm as the data fidelity term. The proposed L1_SRM and L2_SRM models are solved with the SA algorithm. The regularization parameter is selected by the widely used L-curve method for the inversion problem. Synthetic Landsat ETM+, real IKONOS, and real AVIRIS images are used to test the efficacy of the proposed model. LSMA and MESMA algorithms are applied to estimate fraction images. The resultant superresolution land cover map from the proposed model depends on the accuracy of inputted fraction images. Using the L1 or L2 norm as the data fidelity term should depend on fraction error distribution. Moreover, the L-curve method effectively selects the optimal regularization parameter. The accuracy of the resultant superresolution land cover map produced by the proposed SRM model is higher than that of the maps produced by hard classification and several existing SRM algorithms. The Kappa coefficient increases, and the RMSE of the fraction images decreases, showing the effectiveness of the proposed SRM framework.

This proposed framework more effectively solves the SRM problem than existing approaches. However, other possibilities for improvement should still be considered. For example, different data fidelity models can be combined with various land cover spatial pattern models to generate various models under this framework. Some site-specific information can also be incorporated to improve model effectiveness. Moreover, the regularization parameter value selection method should be more comprehensively studied, and a spatial adaptive approach should be explored.

REFERENCES

[1] P. Fisher, "The pixel: A snare and a delusion," *Int. J. Remote Sens.*, vol. 18, no. 3, pp. 679–685, Feb. 1997.
[2] A. P. Cracknell, "Synergy in remote sensing—What's in a pixel?" *Int. J. Remote Sens.*, vol. 19, no. 11, pp. 2025–2047, Jul. 1998.
[3] G. M. Foody, "Status of land cover classification accuracy assessment," *Remote Sens. Environ.*, vol. 80, no. 1, pp. 185–201, Apr. 2002.
[4] N. Keshava and J. F. Mustard, "Spectral unmixing," *IEEE Signal Process. Mag.*, vol. 19, no. 1, pp. 44–57, Jan. 2002.
[5] B. Somers, G. P. Asner, L. Tits, and P. Coppin, "Endmember variability in spectral mixture analysis: A review," *Remote Sens. Environ.*, vol. 115, no. 7, pp. 1603–1616, Jul. 2011.
[6] C. Quintano, A. Fernandez-Manso, Y. E. Shimabukuro, and G. Pereira, "Spectral unmixing," *Int. J. Remote Sens.*, vol. 33, no. 17, pp. 5307–5340, 2012.
[7] A. J. Tatem, H. G. Lewis, P. M. Atkinson, and M. S. Nixon, "Super-resolution target identification from remotely sensed images using a Hopfield neural network," *IEEE Trans. Geosci. Remote Sens.*, vol. 39, no. 4, pp. 781–796, 2001.
[8] K. C. Mertens, L. P. C. Verbeke, E. I. Ducheyne, and R. R. De Wulf, "Using genetic algorithms in sub-pixel mapping," *Int. J. Remote Sens.*, vol. 24, no. 21, pp. 4241–4247, Nov. 2003.
[9] P. M. Atkinson, "Issues of uncertainty in super-resolution mapping and their implications for the design of an inter-comparison study," *Int. J. Remote Sens.*, vol. 30, no. 20, pp. 5293–5308, 2009.
[10] M. W. Thornton, P. M. Atkinson, and D. A. Holland, "Sub-pixel mapping of rural land cover objects from fine spatial resolution satellite sensor imagery using super-resolution swapping," *Int. J. Remote Sens.*, vol. 27, no. 3, pp. 473–491, Feb. 2006.
[11] M. W. Thornton, P. M. Atkinson, and D. A. Holland, "A linearised pixel-swapping method for mapping rural linear land cover features from fine spatial resolution remotely sensed imagery," *Comput. Geosci.*, vol. 33, no. 10, pp. 1261–1272, Oct. 2007.
[12] A. J. Tatem, H. G. Lewis, P. M. Atkinson, and M. S. Nixon, "Increasing the spatial resolution of agricultural land cover maps using a Hopfield neural network," *Int. J Geogr. Inf. Sci.*, vol. 17, no. 7, pp. 647–672, Oct./Nov. 2003.
[13] J. P. Ardila, V. A. Tolpekin, W. Bijker, and A. Stein, "Markov-random-field-based super-resolution mapping for identification of urban trees in VHR images," *ISPRS J. Photogramm. Remote Sens.*, vol. 66, no. 6, pp. 762–775, Nov. 2011.

[14] F. Ling, X. Li, F. Xiao, S. Fang, and Y. Du, "Object-based sub-pixel mapping of buildings incorporating the prior shape information from remotely sensed imagery," *Int. J. Appl. Earth Obs. Geoinf.*, vol. 18, pp. 283–292, Aug. 2012.

[15] G. M. Foody, A. M. Muslim, and P. M. Atkinson, "Super-resolution mapping of the waterline from remotely sensed data," *Int. J. Remote Sens.*, vol. 26, no. 24, pp. 5381–5392, 2005.

[16] A. M. Muslim, G. M. Foody, and P. M. Atkinson, "Localized soft classification for super-resolution mapping of the shoreline," *Int. J. Remote Sens.*, vol. 27, no. 11, pp. 2271–2285, Jun. 2006.

[17] F. Ling, F. Xiao, Y. Du, H. Xue, and X. Ren, "Waterline mapping at the subpixel scale from remote sensing imagery with high-resolution digital elevation models," *Int. J. Remote Sens.*, vol. 29, no. 6, pp. 1809–1815, Mar. 2008.

[18] F. Ling, W. Li, Y. Du, and X. Li, "Land cover change mapping at the subpixel scale with different spatial-resolution remotely sensed imagery," *IEEE Geosci. Remote Sens. Lett.*, vol. 8, no. 1, pp. 182–186, Jan. 2011.

[19] G. M. Foody, "The role of soft classification techniques in the refinement of estimates of ground control point location," *Photogramm. Eng. Remote Sens.*, vol. 68, no. 9, pp. 897–903, Sep. 2002.

[20] X. Li, Y. Du, F. Ling, S. Wu, and Q. Feng, "Using a sub-pixel mapping model to improve the accuracy of landscape pattern indices," *Ecol. Indic.*, vol. 11, no. 5, pp. 1160–1170, Sep. 2011.

[21] Y. Makido and A. Shortridge, "Weighting function alternatives for a subpixel allocation model," *Photogramm. Eng. Remote Sens.*, vol. 73, no. 11, pp. 1233–1240, Nov. 2007.

[22] Y. Makido, A. Shortridge, and J. P. Messina, "Assessing alternatives for modeling the spatial distribution of multiple land-cover classes at subpixel scales," *Photogramm. Eng. Remote Sens.*, vol. 73, no. 8, pp. 935–943, Aug. 2007.

[23] P. M. Atkinson, "Sub-pixel target mapping from soft-classified remotely sensed imagery," *Photogramm. Eng. Remote Sens.*, vol. 71, no. 7, pp. 839–846, Jul. 2005.

[24] F. Ling, X. Li, Y. Du, and F. Xiao, "Sub-pixel mapping of remotely sensed imagery with hybrid intra- and inter-pixel dependence," *Int. J. Remote Sens.*, vol. 34, no. 1, pp. 341–357, Jan. 2013.

[25] A. Boucher and P. C. Kyriakidis, "Super-resolution land cover mapping with indicator geostatistics," *Remote Sens. Environ.*, vol. 104, no. 3, pp. 264–282, Oct. 2006.

[26] A. J. Tatem, H. G. Lewis, P. M. Atkinson, and M. S. Nixon, "Super-resolution land cover pattern prediction using a Hopfield neural network," *Remote Sens. Environ.*, vol. 79, no. 1, pp. 1–14, Jan. 2002.

[27] A. Boucher, "Sub-pixel mapping of coarse satellite remote sensing images with stochastic simulations from training images," *Math. Geosci.*, vol. 41, no. 3, pp. 265–290, Apr. 2009.

[28] A. Boucher, P. C. Kyriakidis, and C. Cronkite-Ratcliff, "Geostatistical solutions for super-resolution land cover mapping," *IEEE Trans. Geosci. Remote Sens.*, vol. 46, no. 1, pp. 272–283, Jan. 2008.

[29] M. Q. Nguyen, P. M. Atkinson, and H. G. Lewis, "Superresolution mapping using a Hopfield neural network with fused images," *IEEE Trans. Geosci. Remote Sensing*, vol. 44, no. 3, pp. 736–749, Mar. 2006.

[30] M. Q. Nguyen, P. M. Atkinson, and H. G. Lewis, "Super-resolution mapping using Hopfield neural network with panchromatic imagery," *Int. J. Remote Sens.*, vol. 32, no. 21, pp. 6149–6176, 2011.

[31] M. Q. Nguyen, P. M. Atkinson, and H. G. Lewis, "Superresolution mapping using a Hopfield neural network with LIDAR data," *IEEE Geosci. Remote Sens. Lett.*, vol. 2, no. 3, pp. 366–370, Jul. 2005.

[32] A. Robin, S. Le Hegarat-Mascle, and L. Moisan, "Unsupervised subpixelic classification using coarse-resolution time series and structural information," *IEEE Trans. Geosci. Remote Sensing*, vol. 46, no. 5, pp. 1359–1374, May 2008.

[33] F. Ling, Y. Du, F. Xiao, H. Xue, and S. Wu, "Super-resolution land-cover mapping using multiple sub-pixel shifted remotely sensed images," *Int. J. Remote Sens.*, vol. 31, no. 19, pp. 5023–5040, Jun. 2010.

[34] A. M. Muad and G. M. Foody, "Super-resolution mapping of lakes from imagery with a coarse spatial and fine temporal resolution," *Int. J. Appl. Earth Obs. Geoinf.*, vol. 15, pp. 79–91, Apr. 2012.

[35] G. M. Foody and H. T. X. Doan, "Variability in soft classification prediction and its implications for sub-pixel scale change detection and super resolution mapping," *Photogramm. Eng. Remote Sens.*, vol. 73, no. 8, pp. 923–933, Aug. 2007.

[36] V. A. Tolpekin and A. Stein, "Quantification of the effects of land-cover-class spectral separability on the accuracy of Markov-random-field-based superresolution mapping," *IEEE Trans. Geosci. Remote Sens.*, vol. 47, no. 9, pp. 3283–3297, Sep. 2009.

[37] F. Ling, Y. Du, X. D. Li, W. B. Li, F. Xiao, and Y. H. Zhang, "Interpolation-based super-resolution land cover mapping," *Remote Sens. Lett.*, vol. 4, no. 7, pp. 629–638, 2013.

[38] K. C. Mertens, L. P. C. Verbeke, T. Westra, and R. R. De Wulf, "Sub-pixel mapping and sub-pixel sharpening using neural network predicted wavelet coefficients," *Remote Sens. Environ.*, vol. 91, no. 2, pp. 225–236, May 2004.

[39] Y. Ge, S. Li, and V. C. Lakhan, "Development and testing of a subpixel mapping algorithm," *IEEE Trans. Geosci. Remote Sensing*, vol. 47, no. 7, pp. 2155–2164, Jul. 2009.

[40] H. Jin, G. Mountrakis, and P. Li, "A super-resolution mapping method using local indicator variograms," *Int. J. Remote Sens.*, vol. 33, no. 24, pp. 7747–7773, 2012.

[41] K. C. Mertens, B. De Baets, L. P. C. Verbeke, and R. R. De Wulf, "A sub-pixel mapping algorithm based on sub-pixel/pixel spatial attraction models," *Int. J. Remote Sens.*, vol. 27, no. 15, pp. 3293–3310, Aug. 2006.

[42] J. Verhoeye and R. De Wulf, "Land cover mapping at sub-pixel scales using linear optimization techniques," *Remote Sens. Environ.*, vol. 79, no. 1, pp. 96–104, Jan. 2002.

[43] Y. Gu, Y. Zhang, and J. Zhang, "Integration of spatial-spectral information for resolution enhancement in hyperspectral images," *IEEE Trans. Geosci. Remote Sens.*, vol. 46, no. 5, pp. 1347–1358, May 2008.

[44] K. Wu, L. Zhang, R. Niu, B. Du, and Y. Wang, "Super-resolution land-cover mapping based on the selective endmember spectral mixture model in hyperspectral imagery," *Opt. Eng.*, vol. 50, no. 12, p. 126201, 2011.

[45] Q. Wang, L. Wang, and D. Liu, "Particle swarm optimization-based sub-pixel mapping for remote-sensing imagery," *Int. J. Remote Sens.*, vol. 33, no. 20, pp. 6480–6496, 2012.

[46] A. Villa, J. Chanussot, J. A. Benediktsson, and C. Jutten, "Spectral unmixing for the classification of hyperspectral images at a finer spatial resolution," *IEEE J. Sel. Topics Signal Process.*, vol. 5, no. 3, pp. 521–533, Jun. 2011.

[47] P. C. Hansen, "Regularization tools version 4.0 for Matlab 7.3," *Numer. Algorithms*, vol. 46, no. 2, pp. 189–194, Oct. 2007.

[48] P. C. Hansen and D. P. Oleary, "The use of the L-curve in the regularization of discrete ill-posed problems," *SIAM J. Sci. Comput.*, vol. 14, no. 6, pp. 1487–1503, Nov. 1993.

[49] D. Calvetti, S. Morigi, L. Reichel, and F. Sgallari, "Tikhonov regularization and the L-curve for large discrete ill-posed problems," *J. Comput. Appl. Math.*, vol. 123, no. 1/2, pp. 423–446, Nov. 2000.

[50] H. Y. Liao and M. K. Ng, "Blind deconvolution using generalized cross-validation approach to regularization parameter estimation," *IEEE Trans. Image Process.*, vol. 20, no. 3, pp. 670–680, Mar. 2011.

[51] M. V. W. Zibetti, F. S. V. Bazan, and J. Mayer, "Determining the regularization parameters for super-resolution problems," *Signal Process.*, vol. 88, no. 12, pp. 2890–2901, Dec. 2008.

[52] T. Kasetkasem, M. K. Arora, and P. K. Varshney, "Super-resolution land cover mapping using a Markov random field based approach," *Remote Sens. Environ.*, vol. 96, no. 3/4, pp. 302–314, Jun. 2005.

[53] X. Li, Y. Du, and F. Ling, "Spatially adaptive smoothing parameter selection for Markov random field based sub-pixel mapping of remotely sensed images," *Int. J. Remote Sens.*, vol. 33, no. 24, pp. 7886–7901, Dec. 2012.

[54] F. Ling, Y. Du, F. Xiao, and X. Li, "Subpixel land cover mapping by integrating spectral and spatial information of remotely sensed imagery," *IEEE Geosci. Remote Sens. Lett.*, vol. 9, no. 3, pp. 408–412, May 2012.

[55] X. Li, F. Ling, and Y. Du, "Super-resolution mapping based on the supervised fuzzy c-means approach," *Remote Sens. Lett.*, vol. 3, no. 6, pp. 501–510, 2012.

[56] S. Farsiu, M. D. Robinson, M. Elad, and P. Milanfar, "Fast and robust multiframe super resolution," *IEEE Trans. Image Process.*, vol. 13, no. 10, pp. 1327–1344, Oct. 2004.

[57] N. Nguyen, P. Milanfar, and G. Golub, "Efficient generalized cross-validation with applications to parametric image restoration and resolution enhancement," *IEEE Trans. Image Process.*, vol. 10, no. 9, pp. 1299–1308, Sep. 2001.

[58] N. Weyrich and G. T. Warhola, "Wavelet shrinkage and generalized cross validation for image denoising," *IEEE Trans. Image Process.*, vol. 7, no. 1, pp. 82–90, Jan. 1998.

[59] L. Bastin, "Comparison of fuzzy c-means classification, linear mixture modelling and MLC probabilities as tools for unmixing coarse pixels," *Int. J. Remote Sens.*, vol. 18, no. 17, pp. 3629–3648, Nov. 1997.

[60] R. L. Powell, D. A. Roberts, P. E. Dennison, and L. L. Hess, "Sub-pixel mapping of urban land cover using multiple endmember spectral mixture analysis: Manaus, Brazil," *Remote Sens. Environ.*, vol. 106, no. 2, pp. 253–267, Jan. 2007.

Feng Ling received the B.S. degree in geology and the M.S. degree in geophysical prospecting and information technology from the Chinese University of Geosciences, Wuhan, China, in 1999 and 2002, respectively, and the Ph.D. degree in system analysis and integration from the Huazhong University of Science and Technology, Wuhan, in 2006.

He is currently an Associate Professor with the Institute of Geodesy and Geophysics, Chinese Academy of Sciences, Wuhan. His research interests are superresolution mapping and uncertainty analysis of remotely sensed imagery.

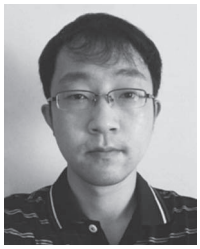

Xiaodong Li received the B.S. degree in geographic information system from the Chinese University of Geosciences, Wuhan, China, in 2006. He received the M.S. and Ph.D. degrees in physical geography from the Institute of Geodesy and Geophysics, Chinese Academy of Sciences, Wuhan, in 2009 and 2012, respectively.

He is currently a Research Assistant with the Institute of Geodesy and Geophysics, Chinese Academy of Sciences, Wuhan. His research interest is superresolution mapping of remotely sensed imagery.

Fei Xiao received the B.S. degree in geology from the Xi'an University of Science and Technology, Xi'an, China, in 2000, the M.S. degree in physical geography from the Institute of Geodesy and Geophysics, Chinese Academy of Sciences, Wuhan, China, in 2003, and the Ph.D. degree in cartography and geographic information system from the Institute of Geographic Sciences and Natural Resources Research, Chinese Academy of Sciences, Beijing, China, in 2006.

He is currently an Associate Professor with the Institute of Geodesy and Geophysics, Chinese Academy of Sciences, Wuhan. His research interests are remote sensing application and geomorphology.

Yun Du received the B.S. degree in geomorphology and quaternary geology from Nanjing University, Nanjing, China, in 1989, the M.S. degree in physical geography from the Institute of Geodesy and Geophysics, Chinese Academy of Sciences, Wuhan, China, in 1992, and the Ph.D. degree in historical geography from Wuhan University, Wuhan, in 1999.

He is currently a Professor with the Institute of Geodesy and Geophysics, Chinese Academy of Sciences, Wuhan. His research interests are remote sensing application and hydrology.